



Multiple odd-parity superconducting phases in bilayer transition metal dichalcogenidesShota Kanasugi ^{1,*} and Youichi Yanase^{1,2}¹*Department of Physics, Kyoto University, Kyoto 606-8502, Japan*²*Institute for Molecular Science, Okazaki 444-8585, Japan* (Received 28 May 2020; revised 17 August 2020; accepted 26 August 2020; published 8 September 2020)

We study unconventional superconductivity in a two-dimensional locally noncentrosymmetric triangular lattice. The model is relevant to bilayer transition metal dichalcogenides with $2H_b$ stacking structure, for example. The superconducting instability is analyzed by solving the linearized Eliashberg equation within the random phase approximation. We show that ferromagnetic fluctuations are dominant owing to the existence of disconnected Fermi pockets near van Hove singularity, and hence odd-parity spin-triplet superconductivity is favored. In the absence of the spin-orbit coupling, we find that odd-parity f -wave superconducting state is stabilized in a wide range of carrier density and interlayer coupling. Furthermore, we investigate impacts of the layer-dependent staggered Rashba and Zeeman spin-orbit coupling on the superconductivity. Multiple odd-parity superconducting phase diagrams are obtained as a function of the spin-orbit coupling and Coulomb interaction. Especially, a topological chiral p -wave pairing state is stabilized in the presence of a moderate Zeeman spin-orbit coupling. Our results shed light on a possibility of odd-parity superconductivity in various ferromagnetic van der Waals materials.

DOI: [10.1103/PhysRevB.102.094507](https://doi.org/10.1103/PhysRevB.102.094507)**I. INTRODUCTION**

Searching for odd-parity superconductors, which provide a platform for the intrinsic topological superconductivity [1–3], has been one of central issues in research field of the unconventional superconductivity. At present, several solid-state materials are proposed as possible candidates for the odd-parity spin-triplet superconductor, e.g., Sr_2RuO_4 [4,5], UPt_3 [6–8], UGe_2 [9], URhGe [10], UCoGe [11], and UTe_2 [12,13]. Note that there are now some results conflicting with the spin-triplet pairing in Sr_2RuO_4 [14–17]. Exploration of spin-triplet superconductivity in systems other than heavy fermions is an important issue.

There are two important factors for realizing spin-triplet pairing states in solid-state materials, i.e., the ferromagnetic (FM) spin fluctuation and the Fermi surface (FS) structure. In the absence of notable FS nesting, the FM fluctuation is enhanced when the Fermi energy lies near the van Hove singularity (vHS). Specifically, the so-called type-II vHS [18–20], whose saddle points are not located at the time-reversal invariant (TRI) momenta, is preferable for the odd-parity superconductivity. On the other hand, a disconnected form of the FS is favorable for the odd-parity pairing since generation of gap nodes is avoidable [21,22]. Stabilization of odd-parity spin-triplet pairing states has been theoretically proposed in a variety of systems with disconnected FSs, e.g., $(\text{TMTSF})_2\text{X}$ ($\text{X} = \text{PF}_6, \text{ClO}_4$) [21,23–26], $\text{Na}_x\text{CoO}_2 \cdot y\text{H}_2\text{O}$ [27–35], SrPtAs [36,37], and doped Kane-Mele model [38]. Note that some experimental results suggest that $\text{Na}_x\text{CoO}_2 \cdot y\text{H}_2\text{O}$ is a spin-singlet superconductor [39,40].

Another intriguing topic for the unconventional superconductivity is the relation between crystalline symmetry and the pairing states [41]. Particularly, various exotic superconducting (SC) phenomena have been elucidated in locally noncentrosymmetric (NCS) systems [42–51], in which the inversion symmetry in a local atomic site is broken although the global inversion symmetry is preserved. Microscopically, a key aspect of locally NCS systems is the sublattice-dependent antisymmetric spin-orbit coupling (SOC), which leads to exotic superconductivity, e.g., singlet-triplet mixed pairing states [44], pair density wave states [46,50], complex stripe states [47], and topological superconductivity [45,48,49]. Especially, it has been clarified that odd-parity topological superconductivity is realized by a combination of antiferromagnetic spin fluctuations and the sublattice-dependent antisymmetric SOC, namely odd-parity magnetic multipole fluctuations [51]. Thus, it is interesting to study interplay of FM-fluctuation-driven superconductivity and locally NCS crystal structure, in the sense of comparison with the case of the antiferromagnetic-fluctuation-driven superconductivity.

Considering the above-mentioned aspects, we provide a thorough microscopic investigation of unconventional superconductivity in a two-dimensional (2D) locally NCS triangular lattice (Fig. 1) with disconnected FSs. The model is relevant to bilayer transition metal dichalcogenides (TMDs) with $2H_b$ stacking structure, which is favored in group-VI TMDs such as MX_2 ($\text{M} = \text{Mo}, \text{W}$ and $\text{X} = \text{S}, \text{Se}$) [52,53]. In a few layer group-VI TMDs, disconnected FSs are formed around K and K' points owing to the triangular lattice structure. Assuming a strong electron correlation, we clarify dominant FM-like spin fluctuations assisted by a type-II vHS. In fact, ferromagnetism has been recently observed in

*kanasugi.shouta.62w@st.kyoto-u.ac.jp

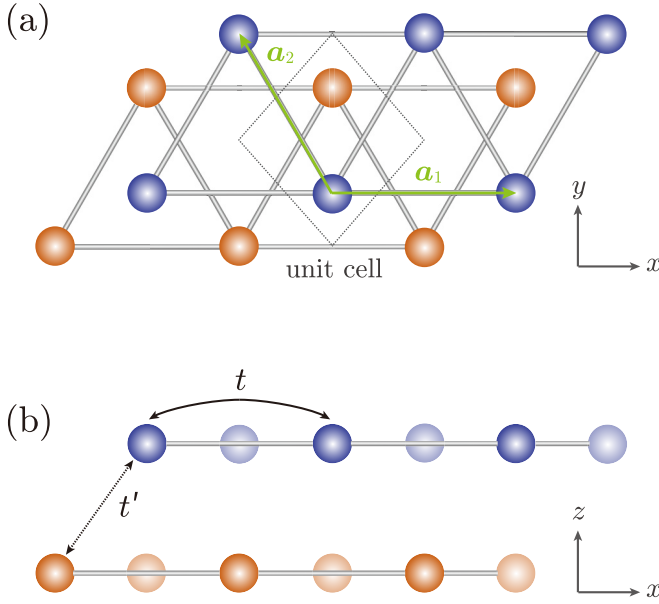


FIG. 1. Crystal structure of the bilayer triangular lattice. (a) The top view and (b) the side view. \mathbf{a}_1 and \mathbf{a}_2 are the lattice vectors. t and t' are the intralayer and interlayer hopping integrals, respectively.

a few-layer VSe₂ [54] and MnSe₂ [55]. Since the conduction electrons in TMDs have d -orbital character, correlation effects are expected to have considerable impacts on the superconductivity [56–59]. We show that odd-parity SC state with f -wave symmetry is stabilized by the FM fluctuation in the absence of the SOC. On the other hand, the local inversion symmetry breaking in the crystal structure induces layer-dependent staggered Rashba and Zeeman SOC. The SOC breaks the spin SU(2) symmetry and lifts the degeneracy of spin-triplet SC states. Thus, the SOC controls the internal degree of freedom of odd-parity superconductivity and its topological property. We elucidate that multiple odd-parity SC phases with either p -wave or f -wave pairing, which belong to different irreducible representations (IRs) of the crystal point group, appear by increasing magnitude of the staggered SOC. It is shown that the multiple SC phase diagram is a consequence of the selection rule for locally NCS superconductors [44] and SOC-induced magnetic anisotropy. In addition, topological properties of the stable odd-parity SC states are studied. A chiral p -wave pairing state in a moderate Zeeman SOC region is identified as a topological SC state in class D.

The rest of the paper is constructed as follows. In Sec. II we introduce a 2D bilayer triangular lattice Hubbard model including the layer-dependent staggered Rashba and Zeeman SOC. The formulation for the microscopic calculations based on the random phase approximation (RPA) and linearized Eliashberg equation is provided. In Sec. III we study the magnetic fluctuations. The dominance of the FM fluctuation and the magnetic anisotropy under the SOC are discussed. Numerical results of the Eliashberg equation are shown in Sec. IV. Stability of f -wave SC states is clarified in the absence of the SOC. In the presence of the SOC, we identify four stable odd-parity SC states with different pairing symmetry. Topological

properties of these SC states are also investigated. Finally, a brief summary and conclusion are provided in Sec. V.

II. MODEL AND FORMULATION

We consider a 2D bilayer triangular lattice with the lattice vectors $\mathbf{a}_1 = (1, 0)$ and $\mathbf{a}_2 = (-1/2, \sqrt{3}/2)$ (Fig. 1), which is classified into D_{3d} point group. The crystal structure is equivalent to that of bilayer TMDs with 2H_b stacking. Recently, superconductivity in bilayer MoS₂ was realized by symmetric gating [60]. On this lattice we introduce a single-orbital Hubbard model $\mathcal{H} = \mathcal{H}_0 + \mathcal{H}_{\text{int}}$. Note that we do not address the multi-orbital physics in this study to perform material-independent general calculations and electron doped MoS₂ is indeed a single-orbital system. The single-particle Hamiltonian \mathcal{H}_0 with SOC is written as

$$\begin{aligned} \mathcal{H}_0 = & \sum_{\mathbf{k}, m, s} (\varepsilon(\mathbf{k}) - \mu) c_{\mathbf{k}, ms}^\dagger c_{\mathbf{k}, ms} \\ & + \sum_{\mathbf{k}, s} (\eta(\mathbf{k}) c_{\mathbf{k}, as}^\dagger c_{\mathbf{k}, bs} + \text{H.c.}) \\ & + \sum_{\mathbf{k}, \zeta, \zeta'} \sum_{j=1,2} \alpha_j \mathbf{g}_j(\mathbf{k}) \cdot \boldsymbol{\sigma}_{ss'} \tau_{mm'}^z c_{\mathbf{k}, ms}^\dagger c_{\mathbf{k}, ms'}, \end{aligned} \quad (1)$$

where $c_{\mathbf{k}, ms}$ is the annihilation operator for an electron with momentum \mathbf{k} and spin $s = \uparrow, \downarrow$ on layer $m = a, b$. $\zeta = (m, s)$ is the abbreviated notation, and σ^μ (τ^ν) is the Pauli matrix for spin (layer) degrees of freedom. The first term is the kinetic energy term. The single-electron kinetic energy is described as

$$\varepsilon(\mathbf{k}) = 2t[\cos \mathbf{k} \cdot \mathbf{a}_1 + \cos \mathbf{k} \cdot \mathbf{a}_2 + \cos \mathbf{k} \cdot (\mathbf{a}_1 + \mathbf{a}_2)], \quad (2)$$

by taking into account the nearest-neighbor hopping. We choose the hopping integral t as a unit of energy ($t = 1$). The chemical potential μ is determined to fix the carrier density as n . The second term is the interlayer coupling. The interlayer hybridization function is given by

$$\eta(\mathbf{k}) = t'[1 + e^{-i\mathbf{k} \cdot \mathbf{a}_2} + e^{-i\mathbf{k} \cdot (\mathbf{a}_1 + \mathbf{a}_2)}]. \quad (3)$$

In this study we assume that the interlayer hopping integral t' is smaller than the intralayer hopping integral t (i.e., $t' < t$). The third term is the layer-dependent staggered SOC, which is originated from the locally NCS crystal structure and a spin-dependent intralayer hopping. Since the local site symmetry is C_{3v} , the g -vector $\mathbf{g}_j(\mathbf{k})$ should belong to A_{2u} IR of D_{3d} which becomes trivial A_1 IR in C_{3v} (see Table I). In this study we consider two kinds of g vectors as

$$\begin{aligned} \mathbf{g}_1(\mathbf{k}) = & \frac{1}{\Lambda} \left[\frac{\sqrt{3}}{2} \{ \sin \mathbf{k} \cdot (\mathbf{a}_1 + \mathbf{a}_2) + \sin \mathbf{k} \cdot \mathbf{a}_2 \} \hat{\mathbf{x}} \right. \\ & \left. - \left\{ \sin \mathbf{k} \cdot \mathbf{a}_1 + \frac{\sin \mathbf{k} \cdot (\mathbf{a}_1 + \mathbf{a}_2) - \sin \mathbf{k} \cdot \mathbf{a}_2}{2} \right\} \hat{\mathbf{y}} \right], \end{aligned} \quad (4)$$

$$\mathbf{g}_2(\mathbf{k}) = \frac{2}{3\sqrt{3}} [\sin \mathbf{k} \cdot \mathbf{a}_1 + \sin \mathbf{k} \cdot \mathbf{a}_2 - \sin \mathbf{k} \cdot (\mathbf{a}_1 + \mathbf{a}_2)] \hat{\mathbf{z}}, \quad (5)$$

TABLE I. 2D basis gap functions for the IRs of trigonal D_{3d} point group without sublattice degrees of freedom. The second column shows the compatibility relations between D_{3d} and C_{3v} .

D_{3d}	$D_{3d} \downarrow C_{3v}$	Basis functions with $k_z = 0$
A_{1g}	A_1	$\bar{\sigma}^0$
A_{2g}	A_2	$k_x k_y (k_x^2 - 3k_y^2)(3k_x^2 - k_y^2) \bar{\sigma}^0$
E_g	E	$\{k_x k_y, k_x^2 - k_y^2\} \bar{\sigma}^0$
A_{1u}	A_2	$k_x \bar{\sigma}^x + k_y \bar{\sigma}^y, k_y (3k_x^2 - k_y^2) \bar{\sigma}^z$
A_{2u}	A_1	$k_x \bar{\sigma}^y - k_y \bar{\sigma}^x, k_x (k_x^2 - 3k_y^2) \bar{\sigma}^z$
E_u	E	$\{k_x \bar{\sigma}^y + k_y \bar{\sigma}^x, k_x \bar{\sigma}^x - k_y \bar{\sigma}^y\}, \{k_x, k_y\} \bar{\sigma}^z$
		$k_x (k_x^2 - 3k_y^2) \{\bar{\sigma}^x, \bar{\sigma}^y\}, k_y (3k_x^2 - k_y^2) \{\bar{\sigma}^x, \bar{\sigma}^y\}$

where $\Lambda = 1.7602$. Equations (4) and (5) are the Rashba and Zeeman SOC, respectively. Both terms belong to A_{2u} IR. The Rashba (Zeeman) SOC originates from the out-of-plane (in-plane) local inversion symmetry breaking at each layer. The constant factors are chosen as $\text{Max}_k |\mathbf{g}_j(\mathbf{k})| = 1$. Although the Rashba SOC is negligible compared to the Zeeman SOC in some TMDs [50,61], we treat both of them on equal footing to provide a general calculation not limited to existing TMDs. The on-site Coulomb interaction is given by

$$\mathcal{H}_{\text{int}} = U \sum_{i,m} n_{i,m\uparrow} n_{i,m\downarrow}, \quad (6)$$

where $n_{i,ms} = c_{i,ms}^\dagger c_{i,ms}$ is the electron density operator on site i . Strong repulsive electron-electron interaction may be present owing to the d -orbital character of conduction carries in TMDs. We treat \mathcal{H}_{int} in the RPA.

We study the SC instability in this model by solving the linearized Eliashberg equation

$$\lambda \Delta_{\xi\xi'}(k) = -\frac{T}{N} \sum_{k'} \sum_{\{\xi_j\}} V_{\xi\xi_1, \xi_2\xi'}(k-k') \times G_{\xi_3\xi_1}(-k') \Delta_{\xi_3\xi_4}(k') G_{\xi_4\xi_2}(k'), \quad (7)$$

where we used the abbreviated notation $k = (\mathbf{k}, i\omega_p)$ and $\omega_p = (2p+1)\pi T$ is the fermionic Matsubara frequency. The noninteracting temperature Green's function is given by $\hat{G}(k) = [i\omega_p \hat{1} - \hat{\mathcal{H}}_0(\mathbf{k})]^{-1}$. λ and $\hat{\Delta}(k)$ are the eigenvalue and gap function, respectively. In the RPA, the effective pairing interaction $\hat{V}(q)$ can be described as

$$\hat{V}(q) = -\hat{\Gamma}^{(0)} \hat{\chi}(q) \hat{\Gamma}^{(0)} - \hat{\Gamma}^{(0)}, \quad (8)$$

by using the RPA susceptibility

$$\hat{\chi}(q) = \hat{\chi}^{(0)}(q) [\hat{1} - \hat{\Gamma}^{(0)} \hat{\chi}^{(0)}(q)]^{-1}. \quad (9)$$

Here the irreducible susceptibility is defined as

$$\chi_{\xi_1\xi_2, \xi_3\xi_4}^{(0)}(q) = -\frac{T}{N} \sum_k G_{\xi_3\xi_1}(k) G_{\xi_2\xi_4}(k+q). \quad (10)$$

The bare irreducible vertex in this model is obtained as

$$\Gamma_{\xi_1\xi_2, \xi_3\xi_4}^{(0)} = \frac{U}{2} \delta_{m_1 m_2} \delta_{m_3 m_4} \delta_{m_1 m_3} \times (\boldsymbol{\sigma}_{s_1 s_2} \cdot \boldsymbol{\sigma}_{s_4 s_3} - \delta_{s_1 s_2} \delta_{s_4 s_3}). \quad (11)$$

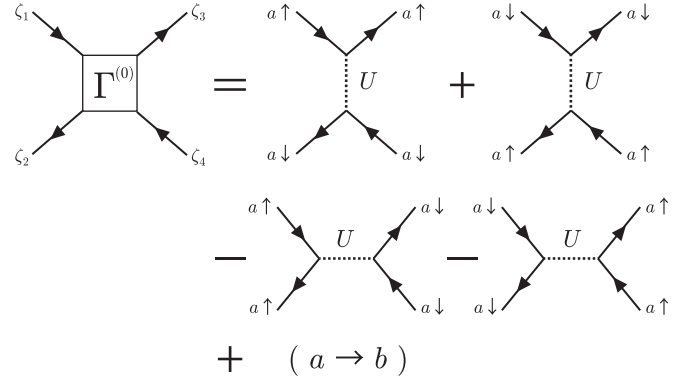


FIG. 2. Diagrammatic representation of the bare irreducible vertex $\hat{\Gamma}^{(0)}$.

The diagrammatic representation of Eq. (11) is shown in Fig. 2. In the following numerical calculations, we set $T/t = 0.02$, 64×64 \mathbf{k} points, and 1024 Matsubara frequencies.

III. MAGNETIC FLUCTUATION

In this section we study the magnetic fluctuation by introducing magnetic susceptibilities as follows:

$$\chi_{mm'}^{\mu\nu}(q) = \sum_{\{s_j\}} \sigma_{s_1 s_2}^\mu \chi_{ms_1 ms_2, m' s_3 m' s_4}(q) \sigma_{s_4 s_3}^\nu, \quad (12)$$

where $\mu, \nu = x, y, z$. The magnetic fluctuation parallel (perpendicular) to the c axis is characterized by $\chi^\parallel \equiv \chi^{zz}$ [$\chi^\perp \equiv (\chi^{xx} + \chi^{yy})/2$]. In the following we consider low doping regimes, in which small disconnected Fermi pockets are formed around the K and K' points [see Fig. 3(a)]. This condition is relevant to electron-doped bilayer TMDs with $2H_b$ stacking structure [60].

First, we investigate the magnetic fluctuations in the absence of the SOC. In this case, there is no magnetic anisotropy, and hence $\chi^\parallel = \chi^\perp (\equiv \chi^S)$. In Figs. 3(b) and 3(c) we show

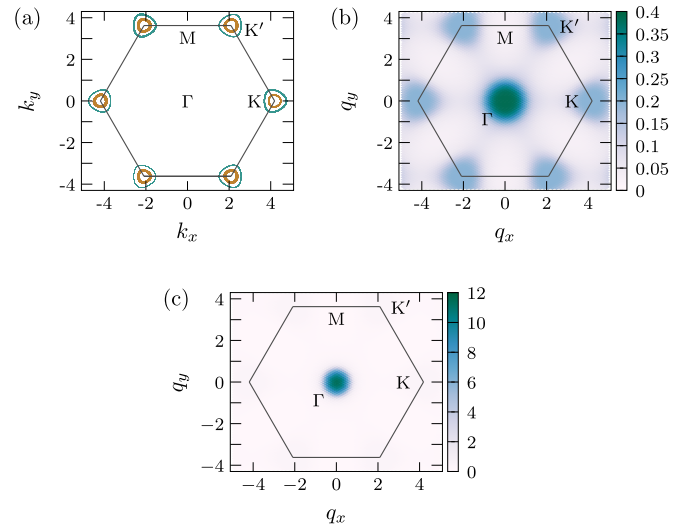


FIG. 3. (a) Fermi surfaces. (b) and (c) Momentum dependence of the intralayer magnetic susceptibility $\chi_{aa(=bb)}^S(\mathbf{q}, 0)$ for (b) $U = 0$ and (c) $U = 5.0$. We set $t'/t = 0.2$, $n = 0.1$, and $\alpha_j = 0$.

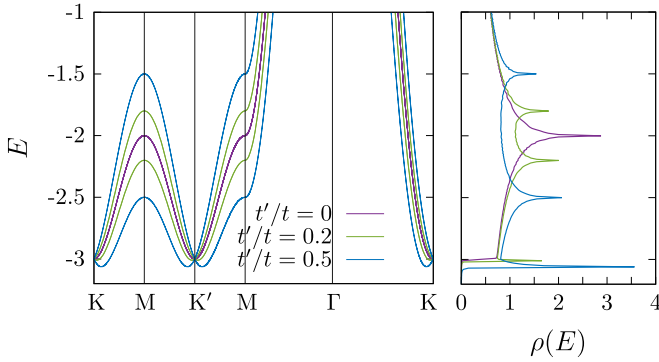


FIG. 4. Band structure and density of states for $\alpha_j = 0$ and $\mu = 0$.

momentum dependence of the intralayer magnetic susceptibility $\chi_{aa}^S (= \chi_{bb}^S)$ for $t'/t = 0.2$, $n = 0.1$ and $\alpha_j = 0$. In the absence of the Coulomb interaction, the magnetic susceptibility takes the maximum value at $\mathbf{q} = \mathbf{0}$ [see Fig. 3(b)] which imply FM spin fluctuation in this system. By introducing the Coulomb interaction, the peak at $\mathbf{q} = \mathbf{0}$ becomes sharper [see Fig. 3(c)], and the FM fluctuation is enhanced. The FM fluctuation is partially owing to the smallness of the FS. Besides, the FM fluctuation is enhanced because the Fermi level lies near the type-II vHS, which is associated with the saddle points located slightly away from the K (K') point. This type-II vHS originates from the band splitting at the band bottom due to a finite interlayer coupling, and hence it is a fingerprint of the bilayer structure. In the $2H_b$ stacking, the interlayer hybridization vanishes at the K (K') points as ensured by the threefold rotational symmetry [53,62,63]. Therefore, Dirac-type linear dispersion appears around the K (K') point (see Fig. 4), and it gives rise to the type-II vHS similar to the Rashba model [64]. Indeed, Fig. 4 reveals a large density of states near the band bottom.

Next, we show the magnetic fluctuations in the presence of the SOC. In locally NCS systems, a sublattice-dependent staggered SOC gives a significant impact on the electronic structure when the ratio of the SOC and the intersublattice coupling is large [43]. Since the interlayer coupling $\eta(\mathbf{k})$ vanishes at the K (K') point [53,62,63], the ratio $\varphi_j(\mathbf{k}) \equiv |\alpha_j \mathbf{g}_j(\mathbf{k})|/|t'\eta(\mathbf{k})|$ can be large on the FS. Hence, the magnetic fluctuation is strongly affected by the staggered SOC. The SOC dependencies of the magnetic susceptibilities are shown in Fig. 5. The sharp peak of the magnetic susceptibility at the Γ point is gradually suppressed by increasing α_j [Figs. 5(a) and 5(c)], and the FM fluctuation is weakened. The suppression of the FM fluctuation is significant in the case of the Zeeman SOC, since the ratio of the SOC and interlayer coupling has a larger value than that in the case of the Rashba SOC [i.e., $\varphi_2(\mathbf{k}_F) > \varphi_1(\mathbf{k}_F)$]. Figures 5(b) and 5(d) reveal appearance of the magnetic anisotropy ($\chi^\parallel \neq \chi^\perp$) owing to the violation of the spin rotational symmetry. The Rashba SOC monotonically increases the magnetic anisotropy mainly at around the Γ point [Fig. 5(b)]. On the other hand, the growth of the magnetic anisotropy by the Zeeman SOC is nonmonotonic [Fig. 5(d)]. Although the SOC dependence of the magnetic anisotropy is complicated, we find that $\chi^\perp > \chi^\parallel$ is always realized at the Γ point. Thus, a FM-like magnetic

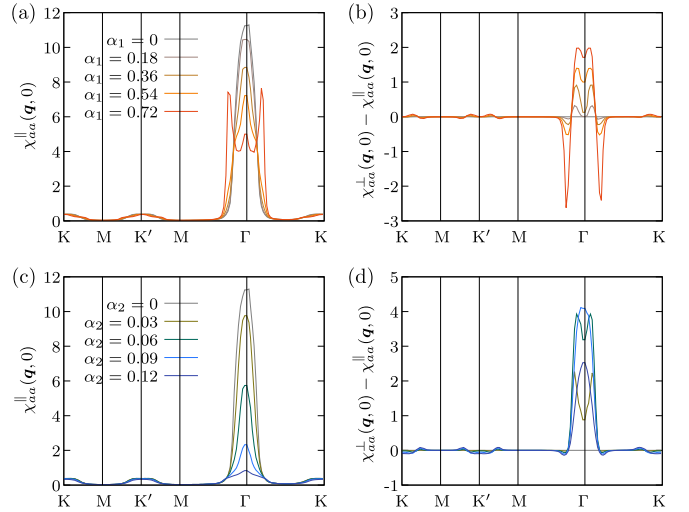


FIG. 5. Momentum dependence of the magnetic susceptibilities along the symmetry axis for several values of (a) and (b) the Rashba SOC α_1 and (c) and (d) Zeeman SOC α_2 . Parameters are set to be $t'/t = 0.2$, $n = 0.1$, $U = 5.0$, and $T = 0.02$. (a) and (c) An intra-layer c -axis component $\chi_{aa}^\parallel(\mathbf{q}, 0)$, and (b) and (d) the anisotropy $\chi_{aa}^\perp(\mathbf{q}, 0) - \chi_{aa}^\parallel(\mathbf{q}, 0)$.

structure with an in-plane spin alignment is favored in the presence of the SOC. It should be noticed that such an in-plane FM ordering has been observed in an atomically thin film of group-V TMD VSe₂ [54]. The superconductivity is significantly affected by this magnetic anisotropy as we demonstrate in Sec. IV B.

IV. SUPERCONDUCTIVITY

Here we illustrate numerical results of the Eliashberg equation in the framework of the RPA. We specify the momentum and layer dependence of the gap functions from the numerical results of the eigenfunctions of the Eliashberg equation. The SC phase diagrams, which illustrate the most stable SC states with the largest eigenvalue, are obtained as a function of the Coulomb interaction, interlayer hopping, carrier density, and SOC. Then, multiple odd-parity SC phases stabilized by FM fluctuations are demonstrated.

A. Superconductivity without spin-orbit coupling

First, we show the SC phases in the absence of the SOC. Figure 6(a) [Fig. 6(b)] shows phase diagrams as a function of the interlayer hopping t' (carrier density n) and Coulomb interaction U at $n = 0.1$ ($t'/t = 0.5$). Owing to the dominant FM spin fluctuations, odd-parity spin-triplet $f_{x(x^2-3y^2)}$ -wave SC states, which are classified into A_{2u} or E_u IRs in the presence of the SOC, are stabilized in the whole parameter region. This $f_{x(x^2-3y^2)}$ -wave SC state is a full gap state and mainly caused by intralayer Cooper pairing. The gap function for the $f_{x(x^2-3y^2)}$ -wave SC state is almost the same as Fig. 10(a). Since the effective pairing interaction for spin-triplet superconductivity is approximated as $V^{\text{triplet}} \simeq -(U^2/2)\chi^S$ in the absence of SOC, the magnetic fluctuation favors the gap function with the same sign on each piece of the FS connected by a vector \mathbf{Q} . Here \mathbf{Q} is the wave vector at which the magnetic susceptibility

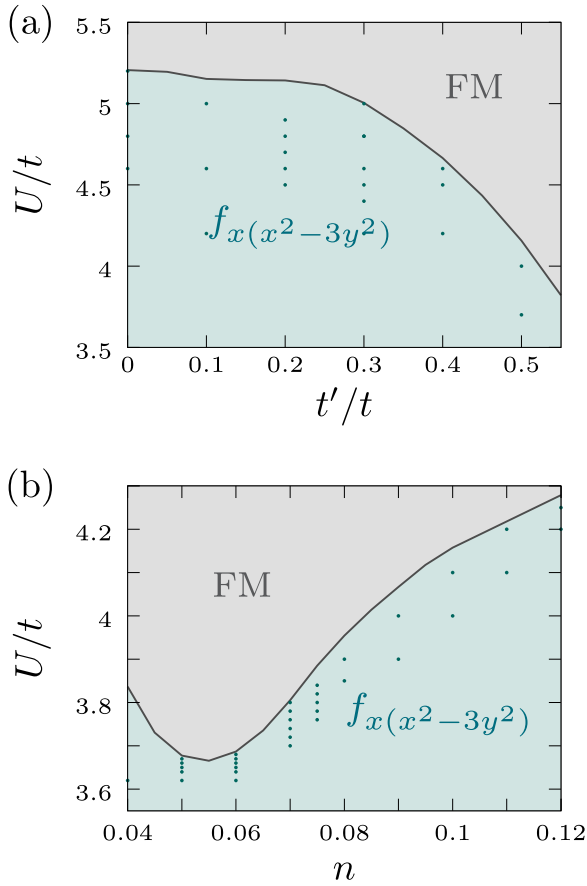


FIG. 6. (a) Phase diagram for the Coulomb interaction U and interlayer hopping t' at $n = 0.1$ and $T = 0.02$. (b) Phase diagram for the Coulomb interaction U and carrier density n at $t'/t = 0.5$ and $T = 0.02$. The solid line is the phase boundary between FM-like ordered state and paramagnetic state, at which the Stoner factor $S = \max[\hat{\Gamma}^{(0)} \hat{\chi}(q)]$ becomes unity. In the paramagnetic phase, the $f_{x(x^2-3y^2)}$ -wave pairing state is stabilized.

is enhanced. As shown in Fig. 3(c), the magnetic susceptibility is sharply peaked at $\mathbf{q} \simeq \mathbf{0}$ (i.e., $\mathbf{Q} \simeq \mathbf{0}$). Thus, the $f_{x(x^2-3y^2)}$ -wave SC state is stabilized to avoid generation of gap nodes at the K and K' points [21,22].

B. Superconductivity and spin-orbit coupling

Next, we investigate superconductivity in the presence of the layer-dependent staggered SOC. In the following discussion we describe the SC gap function as $\Delta_{ms,m's'}^i(k) = \sum_{\mu\nu} d_i^{\mu\nu}(k) \bar{\sigma}_{ss'}^\mu \tau_{mm'}^\nu$, where $i = 1, 2$ is the index for 2D IRs and $\bar{\sigma}_{ss'}^\mu = [\sigma^\mu i \sigma^y]_{ss'}$ ($\mu = 0, x, y, z$). In the presence of the SOC, symmetry of SC states is classified based on the crystallographic point group. Then the gap function belongs to one of IRs of D_{3d} point group shown in Table I. The SC instability is discussed by solving the Eliashberg equation under symmetry constraints for each of the IRs (see Appendix A). Note that the symmetry constraints are technically introduced to avoid numerical errors.

Figure 7 shows the SOC dependence of eigenvalues of the Eliashberg equation λ at $t'/t = 0.2$, $n = 0.1$, and $U = 4.8$. Owing to the dominant FM fluctuation, the intralayer

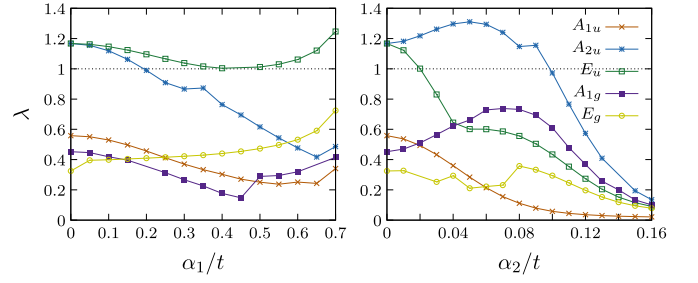


FIG. 7. SOC dependence of eigenvalues of the Eliashberg equation λ at $t'/t = 0.2$, $n = 0.1$, $U = 4.8$, and $T = 0.02$. The eigenvalues for A_{1u} (p -wave), A_{2u} ($f_{x^2(x^2-3y^2)}$ -wave), E_u ($f_{x^2(x^2-3y^2)}$ -wave or p -wave), A_{1g} (s -wave), and E_g (d -wave) pairing states are illustrated.

$f_{x(x^2-3y^2)}$ -wave (A_{2u} or E_u) pairing state is predominant and the p -wave (A_{1u} , A_{2u} , or E_u) pairing state is subdominant for $\alpha_j = 0$. On the other hand, the eigenvalues of even-parity s -wave (A_{1g}) and d -wave (E_g) pairing states are smaller than those of odd-parity pairing states. The eigenvalues of the A_{2u} and E_u SC states are equal at $\alpha_j = 0$, since the spin part of the gap function is threefold degenerated in the absence of the SOC. By turning on the staggered Rashba (Zeeman) SOC, the degeneracy is lifted due to violation of the spin rotational symmetry, and the E_u (A_{2u}) SC state is stabilized as $\lambda^{A_{2u}} < \lambda^{E_u}$ ($\lambda^{A_{2u}} > \lambda^{E_u}$). For these parameters, the spin direction of the SC state is determined by the selection rule for locally NCS superconductors [44,51], which originates from a modulation of the one-particle Green's function by the staggered SOC. The selection rule determines the symmetry of the stable SC state depending on whether the leading SC order parameter is intrasublattice component or intersublattice component (see Fig. 8 for an illustration). For intrasublattice pairing, the spin-singlet SC state or spin-triplet SC state with $\mathbf{d}(\mathbf{k}) \parallel \mathbf{g}(\mathbf{k})$ are stabilized. On the other hand, only the spin-triplet SC state with $\mathbf{d}(\mathbf{k}) \perp \mathbf{g}(\mathbf{k})$ is stable for intersublattice pairing. In a small SOC region, the leading order parameter for

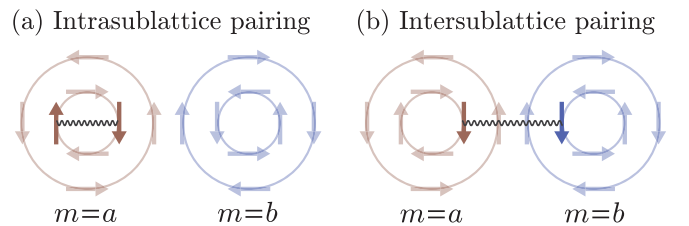


FIG. 8. Schematic figure of the Cooper pairing in a two-sublattice system with the staggered Rashba SOC. The spin texture, which is opposite in each sublattice, can be defined in the absence of intersublattice hybridization as shown in the figure. (a) By choosing the Rashba-type g -vector $\mathbf{g}(\mathbf{k})$ as the spin quantization axis at each momentum, an intrasublattice Cooper pair wave function can be described as $\Psi_{\mathbf{k}}^{\text{intra}} = |\mathbf{k}, \sigma; a\rangle |-\mathbf{k}, \bar{\sigma}; a\rangle$, where $|\mathbf{k}, \sigma; m\rangle$ denotes the wave function for an electron with momentum \mathbf{k} and spin σ on sublattice $m = a, b$. $\Psi_{\mathbf{k}}^{\text{intra}}$ is decomposed to the spin-singlet state and spin-triplet state with $\mathbf{d}(\mathbf{k}) \parallel \mathbf{g}(\mathbf{k})$, and hence only these pairing states are stabilized for intrasublattice pairing. (b) A Cooper pair wave function for the intersublattice pairing state is described as $\Psi_{\mathbf{k}}^{\text{inter}} = |\mathbf{k}, \sigma; a\rangle |-\mathbf{k}, \sigma; b\rangle$. This means that the spin-triplet pairing state with $\mathbf{d}(\mathbf{k}) \perp \mathbf{g}(\mathbf{k})$ is stable for intersublattice pairing.

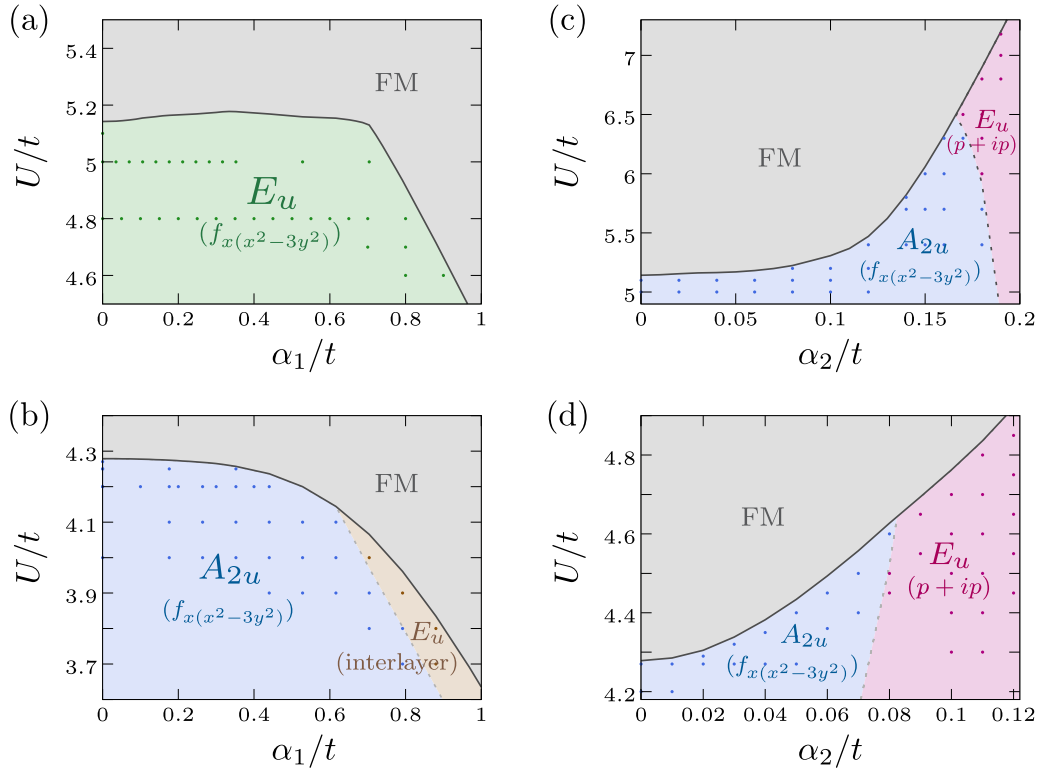


FIG. 9. (a) and (b) Phase diagram for the Coulomb interaction U and staggered Rashba SOC α_1 at $\alpha_2 = 0$ and $T = 0.02$. (c) and (d) Phase diagram for the Coulomb interaction U and staggered Zeeman SOC α_2 at $\alpha_1 = 0$ and $T = 0.02$. (a) and (c) $t'/t = 0.2$ and $n = 0.1$, while (b) and (d) $t'/t = 0.5$ and $n = 0.12$. The solid line is the phase boundary between FM-like ordered state and paramagnetic state. In the paramagnetic phase, the odd-parity A_{2u} and E_u SC states are illustrated.

the A_{2u} (E_u) pairing state possesses the intralayer $f_x(x^2-3y^2)$ -wave symmetry with $\mathbf{d} \parallel \hat{z}$ ($\mathbf{d} \parallel \hat{x}, \hat{y}$). Thus, the A_{2u} (E_u) SC state is destabilized by the staggered Rashba (Zeeman) SOC, since the leading intralayer order parameter with $\mathbf{d} \perp \mathbf{g}_1$ ($\mathbf{d} \perp \mathbf{g}_2$) is incompatible with the selection rule. In addition, to be compatible with the selection rule, the gap function is modified in a large SOC region. For example, the leading order parameter of the E_u pairing state exhibits p -wave symmetry for $\alpha_2/t \gtrsim 0.04$, while that shows $f_x(x^2-3y^2)$ -wave symmetry for $\alpha_2/t \lesssim 0.04$ (see right panel of Fig. 7). As demonstrated above, competition of various SC states with different pairing symmetry can be controlled by the staggered SOC.

The selection rule is derived in the framework of the mean-field theory with assuming a simple pairing interaction [44]. Therefore, it is uncertain whether or not the selection rule holds in the presence of the modification of the effective pairing interaction by the SOC and Coulomb interaction, although it looks to hold in Fig. 7. In order to clarify the applicability of the selection rule in this model, we investigate detailed behaviors of the superconductivity against the staggered SOC and Coulomb interaction in the following part. Figure 9 shows phase diagrams as a function of the staggered SOC α_j and Coulomb interaction U . We found that an odd-parity SC state with either A_{2u} or E_u symmetry is stabilized and it is controlled by magnitude of the SOC and Coulomb interaction. The gap functions for these odd-parity SC states are illustrated in Table II and Figs. 10 and 11. It should be noticed that the Zeeman SOC significantly affects the superconductivity compared to the Rashba SOC because the Zeeman SOC takes a

large magnitude near the K point. Therefore, superconductivity in a trigonal system with in-plane inversion symmetry breaking is affected by a moderate SOC.

In the presence of the Rashba SOC, the superconductivity exhibits different behaviors depending on the magnitude of the interlayer hopping. In the case of a small interlayer hopping $t'/t = 0.2$, the staggered Rashba SOC stabilizes only the E_u SC state [Fig. 9(a)], whose leading order parameters are intralayer spin-triplet components $\{d_1^{y0}, d_2^{x0}\}$ with $f_x(x^2-3y^2)$ -wave symmetry [Figs. 11(a) and 11(b)]. This E_u $f_x(x^2-3y^2)$ -wave SC state is compatible with the selection rule

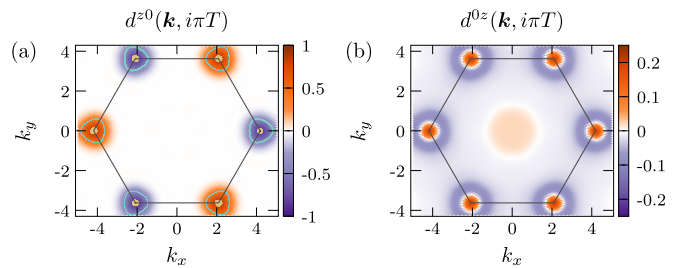


FIG. 10. Gap functions for the A_{2u} SC state at $t'/t = 0.2$, $n = 0.1$, $\alpha_2 = 0.1$, and $U = 5.2$. (a) Leading intralayer $f_x(x^2-3y^2)$ -wave component $d^{z0}(\mathbf{k}, i\pi T)$ and (b) parity-mixing-induced s -wave component $d^{0z}(\mathbf{k}, i\pi T)$. The gap functions are normalized so that the maximum amplitude of the leading order parameter becomes unity. Corresponding FS is illustrated in the left panel. Eigenvalues of the Eliashberg equation is $\lambda = 2.83905$.

TABLE II. Leading order parameters and parity-mixing-induced components for the odd-parity A_{2u} and E_u SC states. $\Delta^s(k)$, $\Delta^{p_x}(k)$, $\Delta^{p_y}(k)$, $\Delta^{d_{x^2-y^2}}(k)$, $\Delta^{d_{xy}}(k)$, and $\Delta^f(k)$ denote gap functions which possess momentum dependence with s -wave, p_x -wave, p_y -wave, $d_{x^2-y^2}$ -wave, d_{xy} -wave, and $f_{x(x^2-3y^2)}$ -wave symmetry. The third column shows the phase diagram in which the corresponding SC state is stabilized. The last column is figures which illustrate the gap functions.

IR	Leading order parameter	Parity mixing	Phase diagram	Gap function
A_{2u}	$\Delta^f(k)\bar{\sigma}^z\tau^0$ $\{\Delta^f(k)\bar{\sigma}^y, \Delta^f(k)\bar{\sigma}^x\}\tau^0$	$\Delta^s(k)\bar{\sigma}^0\tau^z$	Figs. 9(b), 9(c), and 9(d) Fig. 9(a)	Fig. 10 Figs. 11(a) and 11(b)
E_u	$\{\Delta^{p_x}(k), \Delta^{p_y}(k)\}\bar{\sigma}^z\tau^0$ $\{\Delta^f(k)\tau^x, \Delta^f(k)\tau^y\}\bar{\sigma}^z$	$\{\Delta^{d_{x^2-y^2}}(k), \Delta^{d_{xy}}(k)\}\bar{\sigma}^0\tau^z$	Figs. 9(c) and 9(d) Fig. 9(b)	Figs. 11(c) and 11(d) Figs. 11(e) and 11(f)

as we already demonstrate for Fig. 7. On the other hand, in the case of a large interlayer hopping $t'/t = 0.5$, the A_{2u} or E_u SC states are stabilized depending on the magnitude of the Rashba SOC [Fig. 9(b)]. The A_{2u} SC state is favored for a small Rashba SOC region ($0 \lesssim \alpha_1/t \lesssim 0.8$), while the E_u SC state is favored for a large Rashba SOC region ($\alpha_1/t \gtrsim 0.8$). This multiple SC phase diagram is a consequence of competition between the selection rule and magnetic anisotropy. The A_{2u} SC state with the $f_{x(x^2-3y^2)}$ -wave leading order parameter d^{z0}

is incompatible with the selection rule because $\mathbf{d} \perp \mathbf{g}_1$ in the whole Brillouin zone. The stabilization of the A_{2u} SC state may be attributed to the magnetic anisotropy. The magnetic anisotropy under the Rashba SOC is always $\chi^\perp > \chi^\parallel$ near the Γ point like that for $t'/t = 0.2$ [see Fig. 5(b)]. Since the effective pairing interaction for the spin-triplet pair amplitude d^{zv} can be approximated as $V^{\text{eff}} \approx -(U^2/2)(2\chi^\perp - \chi^\parallel)$, the magnetic anisotropy $\chi^\perp > \chi^\parallel$ favors the spin-triplet pairing with $\mathbf{d} \parallel \hat{z}$. Thus, the A_{2u} SC state is stabilized contrary to the selection rule. Note that impacts of a sublattice-dependent staggered SOC on the electronic structure are generally weakened by increasing the intersublattice coupling [43]. Thus, the selection rule is less important for larger t'/t . Leading order parameter of the E_u SC state for $\alpha_1/t \gtrsim 0.8$ is interlayer spin-triplet components $\{d_1^{zx}, d_2^{zy}\}$ [Figs. 11(e) and 11(f)], which are compatible with the selection rule. The enhancement of the interlayer order parameters $\{d_1^{zx}, d_2^{zy}\}$ is attributed to the large interlayer coupling and magnetic anisotropy $\chi^\perp > \chi^\parallel$. Note that the interlayer component of the effective interaction vertex $\hat{V}(q)$ [Eq. (8)] is induced by a finite interlayer hopping contained in the RPA susceptibility $\hat{\chi}(q)$, although the original electron-electron interaction \mathcal{H}_{int} [Eq. (6)] does not couple the layers.

We also investigated superconductivity based on the Kohn-Luttinger framework within the second order perturbation theory [65]. In this approximation, the intrasublattice E_u $f_{x(x^2-3y^2)}$ -wave state is always stable and we do not find violation of the selection rule. This is because the magnetic anisotropy in the bare susceptibility is weak and its effect on superconductivity is negligible. In other words, exchange enhancement of magnetic anisotropy, which is taken into account in the RPA, plays an essential role to stabilize the A_{2u} state violating the selection rule.

On the other hand, the SC phase diagram in the presence of the Zeeman SOC is qualitatively the same irrespective of the magnitude of the interlayer hopping [Figs. 9(c) and 9(d)]. The staggered Zeeman SOC stabilizes the A_{2u} or E_u SC states, depending on magnitude of the Zeeman SOC. The A_{2u} SC state is stabilized in a small Zeeman SOC region, while the E_u SC state is stabilized in a large Zeeman SOC region. Both SC states are indeed compatible with the selection rule. The leading order parameter for the A_{2u} (E_u) SC state is d^{z0} ($\{d_1^{z0}, d_2^{z0}\}$) with $f_{x(x^2-3y^2)}$ -wave (p -wave) symmetry [Fig. 10(a)] [Figs. 11(c) and 11(d)]. Note that the leading order parameter for the E_u SC state changes as $\{d_1^{z0}, d_2^{z0}\}$ ($f_{x(x^2-3y^2)}$ wave) $\rightarrow \{d_1^{zx}, d_2^{zy}\}$ (p wave) by increasing the SOC α_2 so as to be compatible with the selection rule. The

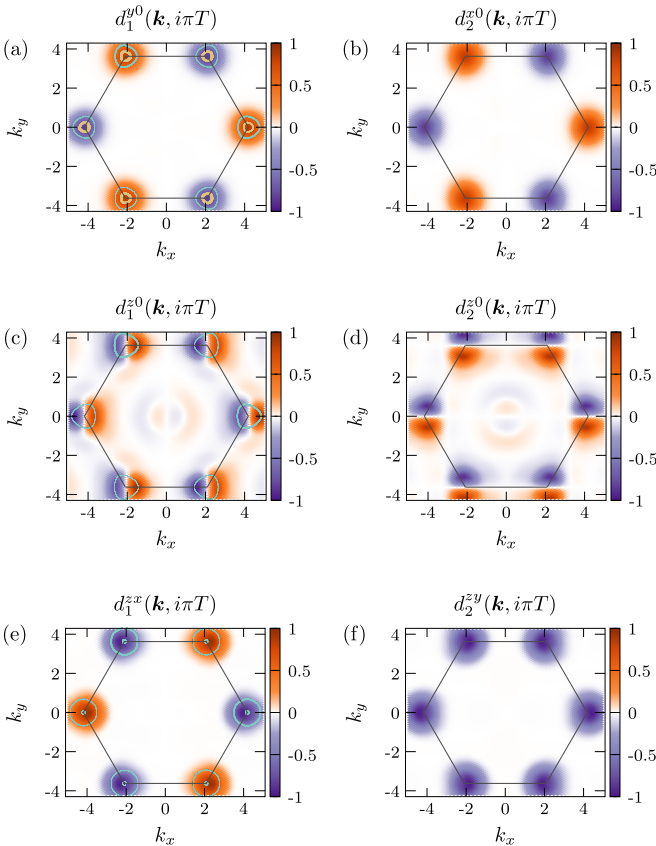


FIG. 11. Leading components of the gap function for the E_u SC states. (a) and (b) $t'/t = 0.2$, $n = 0.1$, $\alpha_1 = 0.35204$, and $U = 5.0$. (c) and (d) $t'/t = 0.2$, $n = 0.1$, $\alpha_2 = 0.19$, and $U = 7.18$. (e) and (f) $t'/t = 0.5$, $n = 0.12$, $\alpha_1 = 0.8801$, and $U = 3.8$. The gap functions are normalized so that the maximum amplitude of the leading order parameter becomes unity. Corresponding FSs are illustrated in the left panels. Eigenvalues of the Eliashberg equation is $\lambda = 2.1145, 1.04829, 2.32491$ in (a) and (b), (c) and (d), and (e) and (f), respectively.

stabilization of the E_u SC state against the A_{2u} SC state may be attributed to the parity-mixing effect for the intralayer pairing. In locally NCS crystals, parity-mixing effect induces an intrasublattice staggered spin-singlet (spin-triplet) component for odd-parity (even-parity) SC states. The symmetry of the parity-mixing-induced component is determined by the compatibility relation between the global symmetry and the local site symmetry. In our model, the global and local site symmetries are classified as D_{3d} and C_{3v} , respectively. Then the parity-mixing occurs between A_{1g} and A_{2u} , A_{2g} and A_{1u} , and E_g and E_u (see second column of Table I) at each layer. As shown in Fig. 10, the parity mixing effect induces an s -wave component d^{0z} in the A_{2u} SC state, and it becomes comparable to the leading $f_{x(x^2-3y^2)}$ -wave component d^{x0} in the large Zeeman SOC region. On the other hand, an intrasublattice staggered d -wave component (not shown) appears in the E_u SC state as a consequence of the parity-mixing effect. Since the s -wave pairing is unfavorable in the presence of the Coulomb interaction, the strongly parity-mixed $f + s$ -wave A_{2u} SC state is overwhelmed by the $p + d$ -wave E_u SC state in the large Zeeman SOC region. The critical value $\alpha_2 \sim 0.1$ corresponds to $\alpha_2 = 20$ meV when we adopt $t = 200$ meV [53]. This value lies in the realistic range of TMDs. Finally, we note that the competition between the selection rule and magnetic anisotropy does not occur in the case of the Zeeman SOC, in contrast to the case of the Rashba SOC.

C. Topological superconductivity

Finally, we discuss topological superconductivity. The \mathbb{Z}_2 part of topological invariants for the odd-parity SC states is determined by the occupation numbers at the TRI momenta in the Brillouin zone [1–3]. In our model, the number of disconnected FSs enclosing the TRI momenta (Γ and M points) is even. Thus the \mathbb{Z}_2 invariant for a TRI odd-parity SC state (DIII class) is trivial. The SC states that belong to one-dimensional IRs do not break the time-reversal symmetry, and hence the A_{1u} and A_{2u} SC states are topologically trivial.

On the other hand, the SC states classified into 2D IRs may realize spontaneous time-reversal symmetry breaking, depending on the superposition of two gap functions. Then the integer topological invariant (Chern number in class D) can be a nonzero even number. For instance, the E_u p -wave SC state in a large Zeeman SOC region [Figs. 9(c) and 9(d)] should be a chiral $p_x + ip_y$ pairing state in order to fully gap out the FS [i.e., the order parameter is written as $\sim(\Delta^{p_x} \pm i\Delta^{p_y})\bar{\sigma}^z\tau^0$]. This E_u $p_x + ip_y$ -wave pairing state is identified as a topological SC state in class D with the Chern number $\nu_{\text{Ch}} = \pm 4$ (see Appendix B). A similar topological SC state is proposed in monolayer TMDs [59], while it is a parity-mixed chiral $p + d$ -wave pairing state owing to violation of the global inversion symmetry.

In contrast, the E_u f -wave SC states under the Rashba SOC do not break the time-reversal symmetry, and therefore, they are topologically trivial. In order to fully gap out the FS, indeed, the order parameter for the E_u $f_{x(x^2-3y^2)}$ -wave pairing state [Fig. 9(a)] should be $\sim\Delta^f(\bar{\sigma}^x \pm \bar{\sigma}^y)\tau^0$, while that for the E_u interlayer pairing state [Fig. 9(b)] should be $\sim(\Delta^f\tau^x \pm \Delta^f\tau^y)\bar{\sigma}^z$. Time-reversal symmetry is preserved, while these

states may realize nematic superconductivity with spontaneous rotation symmetry breaking. When we assume superposition breaking the time-reversal symmetry, the nonunitary SC state gains less condensation energy, and it is unstable.

V. SUMMARY AND DISCUSSION

In summary, we have studied unconventional superconductivity in a 2D locally NCS triangular lattice, which is relevant to the crystal structure of bilayer TMDs with $2H_b$ stacking. By assuming disconnected FSs and strong electron correlation, we have clarified the dominant FM spin fluctuations on the basis of the RPA. The significant enhancement of the FM fluctuation is assisted by the type-II vHS due to a finite interlayer coupling, and hence it is a characteristic of the bilayer structure. The SC instability has been discussed based on the analysis of the linearized Eliashberg equation. The odd-parity spin-triplet superconductivity is favored by the FM fluctuation, and we found that fully gapped f -wave pairing state is stabilized in a wide range of the interlayer coupling and carrier density. Furthermore, impacts of the staggered Rashba or Zeeman antisymmetric SOC on the magnetic fluctuation and superconductivity have been elucidated. The magnetic anisotropy is enhanced by increasing the SOC, and a FM-like magnetic structure with in-plane spin alignment, such as in a few-layer VSe₂ [54], is favored by either Rashba or Zeeman SOC. We found that the odd-parity A_{2u} or E_u SC states with either f -wave or p -wave gap functions are stabilized depending on magnitude of the SOC, interlayer hopping, and Coulomb interaction. The stability of each odd-parity SC states is determined by a combination of the selection rule for locally NCS superconductors [44,51], magnetic anisotropy, and parity-mixing effect in the SC state. In addition, topological properties of the stable odd-parity pairing states have been studied based on the FS formula [1–3] and estimation of topological invariants. Then, the E_u $p + ip$ -wave pairing state has been identified as a topological SC state in class D with the Chern number $\nu_{\text{Ch}} = 4$. This state is stabilized by a moderate Zeeman SOC realistic in TMDs.

Our results suggest odd-parity superconductivity ubiquitous in $2H_b$ -stacked bilayer TMDs, such as bilayer MoS₂ in which gate-induced superconductivity is realized [60,66]. An essential ingredient for the odd-parity superconductivity is underlying FM fluctuations induced by a strong electron correlation. Although dominance of the electron-phonon coupling for the superconductivity in a few-layer TMDs is proposed by some theoretical studies [67–69], the electron-electron interaction is also expected to affect the superconductivity owing to the d -orbital character of carriers in TMDs [56–59]. Indeed, a recent tunneling spectroscopy measurement for monolayer MoS₂ has revealed anisotropic SC gap, which suggests that the microscopic origin of the superconductivity cannot be captured by a conventional phonon-driven mechanism [70]. Thus, various bilayer TMDs have a potential for hosting FM fluctuations and odd-parity superconductivity. This study clarifies a way to control odd-parity SC phases by SOC and carrier doping, and to realize topological superconductivity in 2D TMDs.

Our study also sheds light on a possibility of odd-parity superconductivity in a variety of 2D magnetic van der Waals

materials [71] not only TMDs. In van der Waals materials, strong enhancement of spin fluctuations, which potentially leads to unconventional superconductivity, is expected owing to the 2D nature. In fact, ferromagnetism has been detected in atomically thin film of CrI₃ [72], Cr₂Ge₂Te₆ [73], VSe₂ [54], V₅Se₈ [74], and MnSe_x [55]. Such FM van der Waals materials may offer a platform for multiple odd-parity SC phases.

ACKNOWLEDGMENTS

The authors are grateful to J. Ishizuka, S. Sumita, Q. Chen, and J. Ye for helpful discussions. This work was supported by JSPS KAKENHI (Grants No. JP15H05884, No. JP18H04225, No. JP18H05227, No. JP18H01178, and No. 20H05159). S.K. is supported by a JSPS research fellowship and by JSPS KAKENHI (Grant No. 19J22122).

APPENDIX A: SYMMETRY OF SUPERCONDUCTING STATES

In this Appendix we study symmetry constraints for SC states. First, we consider transformation of the Bloch state under space group operations. A creation operator of a Bloch state with spin s on layer m is defined as

$$c_{\mathbf{k},ms}^\dagger = \sum_{\mathbf{R}} c_s^\dagger(\mathbf{R} + \mathbf{r}_m) e^{-i\mathbf{k}\cdot\mathbf{R}}, \quad (\text{A1})$$

where \mathbf{R} represents the position for the unit cell and \mathbf{r}_m is the relative position of the layer m in a unit cell. Using Eq. (A1), the creation operator is transformed by a space group operation $g = \{p|\mathbf{a}\}$ as follows:

$$\begin{aligned} g c_{\mathbf{k},ms}^\dagger g^{-1} &= \sum_{\mathbf{R}} g c_s^\dagger(\mathbf{R} + \mathbf{r}_m) g^{-1} e^{-i\mathbf{k}\cdot\mathbf{R}} \\ &= \sum_{\mathbf{R}} e^{-i\mathbf{k}\cdot\mathbf{R}} \sum_{s'} c_{s'}^\dagger(p(\mathbf{R} + \mathbf{r}_m) + \mathbf{a}) D_{s's}^{(1/2)}(p), \end{aligned} \quad (\text{A2})$$

where $D^{(1/2)}(p)$ is a representation matrix of the point group operation p in the spin space. By defining $\mathbf{R}' + \mathbf{r}_{pm} \equiv p(\mathbf{R} + \mathbf{r}_m) + \mathbf{a}$, Eq. (A2) is rewritten as

$$\begin{aligned} g c_{\mathbf{k},ms}^\dagger g^{-1} &= \sum_{\mathbf{R}'} e^{-i\mathbf{k}\cdot[p^{-1}(\mathbf{R}' + \mathbf{r}_{pm} - \mathbf{a})]} \\ &\times \sum_{s'} c_{s'}^\dagger(\mathbf{R}' + \mathbf{r}_{pm}) D_{s's}^{(1/2)}(p) \\ &= e^{i\mathbf{p}\mathbf{k}\cdot\mathbf{a}} \sum_{m',s'} c_{\mathbf{p}\mathbf{k},m's'}^\dagger D_{m'm,\mathbf{k}}^{(\text{perm})}(p, \mathbf{k}) D_{s's}^{(1/2)}(p). \end{aligned} \quad (\text{A3})$$

Here we introduced a representation matrix for the permutation of layers as

$$D_{m'm}^{(\text{perm})}(p, \mathbf{k}) = e^{-i\mathbf{p}\mathbf{k}\cdot(\mathbf{r}_{pm} - \mathbf{p}\mathbf{r}_m)} \delta_{m',pm}. \quad (\text{A4})$$

We investigate the symmetry of SC states based on the pair amplitude

$$F_{ms,m's'}(\mathbf{k}) = \langle c_{\mathbf{k},ms} c_{-\mathbf{k},m's'} \rangle, \quad (\text{A5})$$

which satisfies the fermionic antisymmetry

$$F_{ms,m's'}(\mathbf{k}) = -F_{m's',ms}(-\mathbf{k}). \quad (\text{A6})$$

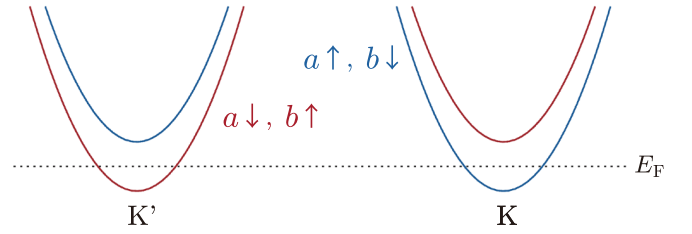


FIG. 12. Schematic of the band structure near the K and K' points in a large Zeeman SOC region. The Fermi energy E_F lies between the Zeeman gap.

From Eq. (A3) it is revealed that the pair amplitude is transformed by a space group operation g as

$$\begin{aligned} g F_{ms,m's'}^\Gamma(\mathbf{k}) g^{-1} &= \sum_{\{m_j, s_j\}} F_{m_1 s_1, m_2 s_2}^\Gamma(p\mathbf{k}) D^\Gamma(g) \\ &\times \mathcal{D}_{m_1 m_2, m m'}^{(\text{perm})}(p, \mathbf{k}) \mathcal{D}_{s_1 s_2, s s'}^{(1/2)}(p), \end{aligned} \quad (\text{A7})$$

where the representation matrices are introduced as

$$\mathcal{D}_{m_1 m_2, m m'}^{(\text{perm})}(p, \mathbf{k}) = D_{m_1 m}^{(\text{perm})}(p, \mathbf{k}) D_{m_2 m'}^{(\text{perm})}(p, -\mathbf{k}), \quad (\text{A8})$$

$$\mathcal{D}_{s_1 s_2, s s'}^{(1/2)}(p) = D_{s_1 s}^{(1/2)}(p) D_{s_2 s'}^{(1/2)}(p), \quad (\text{A9})$$

and $D^\Gamma(g)$ is the representation matrix of the Γ IR for the gap function. Whereas $D^\Gamma(g) = \pm 1$ for one-dimensional IRs, $D^\Gamma(g)$ is 2×2 matrix for 2D IRs. Equations (A6) and (A7) are the symmetry constraints for the SC states. In the main text, the linearized Eliashberg equation is solved under these symmetry constraints for each of the IRs of D_{3d} point group.

APPENDIX B: CHERN NUMBER FOR E_u PAIRING STATE

Here we derive the Chern number for the E_u $p_x + ip_y$ -wave pairing state in a large Zeeman SOC region [Figs. 9(c) and 9(d)]. Figure 12 illustrates the band structure near the Fermi level under a large Zeeman SOC. Since the fourfold degeneracy at the K (K') point is lifted by the Zeeman SOC, the band structure possesses a nearly parabolic shape around the K (K') point. In addition, the interlayer hybridization is negligible around the K (K') point owing to the threefold rotational symmetry [53,62,63]. Then the effective Hamiltonian for electrons near the Fermi level is derived as

$$\begin{aligned} \tilde{\mathcal{H}} &= \sum_{\mathbf{q}, m, s} (\tilde{\epsilon}_{\mathbf{q}} - \mu) \psi_{\mathbf{q}, ms}^\dagger \psi_{\mathbf{q}, ms} \\ &+ \frac{1}{2} \sum_{\mathbf{q}, m, s, s'} \tilde{\Delta}_{\mathbf{q}} \tilde{\sigma}_{ss'}^z \psi_{\mathbf{q}, ms}^\dagger \psi_{-\mathbf{q}, ms'}^\dagger + \text{H.c.}, \end{aligned} \quad (\text{B1})$$

where $\tilde{\epsilon}_{\mathbf{q}} = \mathbf{q}^2/(2m)$ is the effective kinetic energy with a parabolic dispersion, $\tilde{\Delta}_{\mathbf{q}} = \tilde{\Delta}^p(q_x + iq_y)$ is the effective chiral p -wave gap function, and the annihilation operators are defined as $(\psi_{\mathbf{q}, a\uparrow}, \psi_{\mathbf{q}, a\downarrow}, \psi_{\mathbf{q}, b\uparrow}, \psi_{\mathbf{q}, b\downarrow}) \equiv (c_{\mathbf{K}+\mathbf{q}, a\uparrow}, c_{-\mathbf{K}+\mathbf{q}, a\downarrow}, c_{-\mathbf{K}+\mathbf{q}, b\uparrow}, c_{\mathbf{K}+\mathbf{q}, b\downarrow})$. We assume that $\tilde{\Delta}^p$ is a real number. By using the vector operator

$$\hat{\Psi}_{\mathbf{q}, m}^\dagger = (\psi_{\mathbf{q}, m\uparrow}^\dagger, \psi_{-\mathbf{q}, m\uparrow}^\dagger, \psi_{\mathbf{q}, m\downarrow}^\dagger, \psi_{-\mathbf{q}, m\downarrow}^\dagger), \quad (\text{B2})$$

we obtain the matrix representation of the effective Hamiltonian as follows:

$$\tilde{\mathcal{H}} = \frac{1}{2} \sum_q (\hat{\Psi}_{q,a}^\dagger, \hat{\Psi}_{q,b}^\dagger) \tilde{\mathcal{H}}_q \begin{pmatrix} \hat{\Psi}_{q,a} \\ \hat{\Psi}_{q,b} \end{pmatrix} + \text{const.}, \quad (\text{B3})$$

where the Hamiltonian matrix $\tilde{\mathcal{H}}_q$ is given by

$$\tilde{\mathcal{H}}_q = \tau^0 \otimes \begin{pmatrix} (\tilde{\epsilon}_q - \mu)\sigma^z & \tilde{\Delta}^p(q_x\sigma^x - q_y\sigma^y) \\ \tilde{\Delta}^p(q_x\sigma^x - q_y\sigma^y) & (\tilde{\epsilon}_q - \mu)\sigma^z \end{pmatrix}. \quad (\text{B4})$$

Here we carry out an unitary transformation as

$$U \tilde{\mathcal{H}}_q U^\dagger = \tau^0 \otimes \begin{pmatrix} \tilde{\mathcal{H}}_q^+ & 0 \\ 0 & \tilde{\mathcal{H}}_q^- \end{pmatrix}, \quad (\text{B5})$$

$$\tilde{\mathcal{H}}_q^\pm = \begin{pmatrix} \tilde{\epsilon}_q - \mu & \pm \tilde{\Delta}^p(q_x + iq_y) \\ \pm \tilde{\Delta}^p(q_x - iq_y) & -\tilde{\epsilon}_q + \mu \end{pmatrix}, \quad (\text{B6})$$

where the unitary matrix U is defined as

$$U = \frac{1}{\sqrt{2}} \tau^0 \otimes \begin{pmatrix} \sigma^0 & \sigma^0 \\ \sigma^0 & -\sigma^0 \end{pmatrix}. \quad (\text{B7})$$

Equation (B6) is the Bogoliubov–de Gennes Hamiltonian for the spinless chiral p -wave superconductivity. Thus, the spinful chiral p -wave SC state is converted to two pairs of the spinless chiral p -wave SC states [59]. Since a spinless chiral p -wave SC state gives the Chern number 1, the total Chern number of the E_u chiral p -wave SC state is obtained as $\nu_{\text{Ch}} = 1 \times 2 \times 2 = 4$.

-
- [1] M. Sato, *Phys. Rev. B* **79**, 214526 (2009).
[2] M. Sato, *Phys. Rev. B* **81**, 220504(R) (2010).
[3] L. Fu and E. Berg, *Phys. Rev. Lett.* **105**, 097001 (2010).
[4] T. M. Rice and M. Sigrist, *J. Phys.: Condens. Matter* **7**, L643 (1995).
[5] A. P. Mackenzie and Y. Maeno, *Rev. Mod. Phys.* **75**, 657 (2003).
[6] J. A. Sauls, *Adv. Phys.* **43**, 113 (1994).
[7] H. Tou, Y. Kitaoka, K. Ishida, K. Asayama, N. Kimura, Y. Onuki, E. Yamamoto, Y. Haga, and K. Maezawa, *Phys. Rev. Lett.* **80**, 3129 (1998).
[8] R. Joynt and L. Taillefer, *Rev. Mod. Phys.* **74**, 235 (2002).
[9] S. Saxena, P. Agarwal, K. Ahilan, F. Grosche, R. Haselwimmer, M. Steiner, E. Pugh, I. Walker, S. Julian, P. Monthoux *et al.*, *Nature (London)* **406**, 587 (2000).
[10] D. Aoki, A. Huxley, E. Ressouche, D. Braithwaite, J. Flouquet, J.-P. Brison, E. Lhotel, and C. Paulsen, *Nature (London)* **413**, 613 (2001).
[11] N. T. Huy, A. Gasparini, D. E. de Nijs, Y. Huang, J. C. P. Klaasse, T. Gortenmulder, A. de Visser, A. Hamann, T. Görlach, and H. v. Löhneysen, *Phys. Rev. Lett.* **99**, 067006 (2007).
[12] S. Ran, C. Eckberg, Q.-P. Ding, Y. Furukawa, T. Metz, S. R. Saha, I.-L. Liu, M. Zic, H. Kim, J. Paglione *et al.*, *Science* **365**, 684 (2019).
[13] D. Aoki, A. Nakamura, F. Honda, D. Li, Y. Homma, Y. Shimizu, Y. J. Sato, G. Knebel, J.-P. Brison, A. Pourret *et al.*, *J. Phys. Soc. Jpn.* **88**, 043702 (2019).
[14] S. Yonezawa, T. Kajikawa, and Y. Maeno, *J. Phys. Soc. Jpn.* **83**, 083706 (2014).
[15] S. Kittaka, A. Kasahara, T. Sakakibara, D. Shibata, S. Yonezawa, Y. Maeno, K. Tenya, and K. Machida, *Phys. Rev. B* **90**, 220502(R) (2014).
[16] A. Pustogow, Y. Luo, A. Chronister, Y.-S. Su, D. Sokolov, F. Jerzembeck, A. P. Mackenzie, C. Hicks, N. Kikugawa, S. Raghu *et al.*, *Nature (London)* **574**, 72 (2019).
[17] K. Ishida, M. Manago, K. Kinjo, and Y. Maeno, *J. Phys. Soc. Jpn.* **89**, 034712 (2020).
[18] H. Yao and F. Yang, *Phys. Rev. B* **92**, 035132 (2015).
[19] Z. Y. Meng, F. Yang, K.-S. Chen, H. Yao, and H.-Y. Kee, *Phys. Rev. B* **91**, 184509 (2015).
[20] X. Wu, M. Fink, W. Hanke, R. Thomale, and D. Di Sante, *Phys. Rev. B* **100**, 041117(R) (2019).
[21] K. Kuroki, R. Arita, and H. Aoki, *Phys. Rev. B* **63**, 094509 (2001).
[22] K. Kuroki and R. Arita, *Phys. Rev. B* **63**, 174507 (2001).
[23] Y. Tanaka and K. Kuroki, *Phys. Rev. B* **70**, 060502(R) (2004).
[24] K. Kuroki and Y. Tanaka, *J. Phys. Soc. Jpn.* **74**, 1694 (2005).
[25] J. C. Nickel, R. Duprat, C. Bourbonnais, and N. Dupuis, *Phys. Rev. Lett.* **95**, 247001 (2005).
[26] Y. Fuseya and Y. Suzumura, *J. Phys. Soc. Jpn.* **74**, 1263 (2005).
[27] K. Kuroki, Y. Tanaka, and R. Arita, *Phys. Rev. Lett.* **93**, 077001 (2004).
[28] K. Kuroki, Y. Tanaka, and R. Arita, *Phys. Rev. B* **71**, 024506 (2005).
[29] H. Ikeda, Y. Nisikawa, and K. Yamada, *J. Phys. Soc. Jpn.* **73**, 17 (2004).
[30] Y. Tanaka, Y. Yanase, and M. Ogata, *J. Phys. Soc. Jpn.* **73**, 319 (2004).
[31] Y. Nisikawa, H. Ikeda, and K. Yamada, *J. Phys. Soc. Jpn.* **73**, 1127 (2004).
[32] Y. Yanase, M. Mochizuki, and M. Ogata, *J. Phys. Soc. Jpn.* **74**, 430 (2005).
[33] Y. Yanase, M. Mochizuki, and M. Ogata, *J. Phys. Soc. Jpn.* **74**, 2568 (2005).
[34] I. Mazin and M. Johannes, *Nat. Phys.* **1**, 91 (2005).
[35] M. Mochizuki, Y. Yanase, and M. Ogata, *Phys. Rev. Lett.* **94**, 147005 (2005).
[36] J. Goryo, M. H. Fischer, and M. Sigrist, *Phys. Rev. B* **86**, 100507(R) (2012).
[37] W.-S. Wang, Y. Yang, and Q.-H. Wang, *Phys. Rev. B* **90**, 094514 (2014).
[38] Y. Fukaya, K. Yada, A. Hattori, and Y. Tanaka, *J. Phys. Soc. Jpn.* **85**, 104704 (2016).
[39] G.-q. Zheng, K. Matano, D. P. Chen, and C. T. Lin, *Phys. Rev. B* **73**, 180503(R) (2006).
[40] K. Matano, G.-Q. Zheng, D. Chen, and C. Lin, *Phys. B: Condens. Matter* **403**, 1107 (2008).
[41] M. Sigrist and K. Ueda, *Rev. Mod. Phys.* **63**, 239 (1991).
[42] M. Sigrist, D. F. Agterberg, M. H. Fischer, J. Goryo, F. Loder, S.-H. Rhim, D. Maruyama, Y. Yanase, T. Yoshida, and S. J. Youn, *J. Phys. Soc. Jpn.* **83**, 061014 (2014).
[43] D. Maruyama, M. Sigrist, and Y. Yanase, *J. Phys. Soc. Jpn.* **81**, 034702 (2012).

- [44] M. H. Fischer, F. Loder, and M. Sigrist, *Phys. Rev. B* **84**, 184533 (2011).
- [45] S. Nakosai, Y. Tanaka, and N. Nagaosa, *Phys. Rev. Lett.* **108**, 147003 (2012).
- [46] T. Yoshida, M. Sigrist, and Y. Yanase, *Phys. Rev. B* **86**, 134514 (2012).
- [47] T. Yoshida, M. Sigrist, and Y. Yanase, *J. Phys. Soc. Jpn.* **82**, 074714 (2013).
- [48] T. Yoshida, M. Sigrist, and Y. Yanase, *Phys. Rev. Lett.* **115**, 027001 (2015).
- [49] T. Yoshida, A. Daido, Y. Yanase, and N. Kawakami, *Phys. Rev. Lett.* **118**, 147001 (2017).
- [50] Y. Nakamura and Y. Yanase, *Phys. Rev. B* **96**, 054501 (2017).
- [51] J. Ishizuka and Y. Yanase, *Phys. Rev. B* **98**, 224510 (2018).
- [52] J. A. Wilson and A. Yoffe, *Adv. Phys.* **18**, 193 (1969).
- [53] G.-B. Liu, D. Xiao, Y. Yao, X. Xu, and W. Yao, *Chem. Soc. Rev.* **44**, 2643 (2015).
- [54] M. Bonilla, S. Kolekar, Y. Ma, H. C. Diaz, V. Kalappattil, R. Das, T. Eggers, H. R. Gutierrez, M.-H. Phan, and M. Batzill, *Nat. Nanotechnol.* **13**, 289 (2018).
- [55] D. J. OHara, T. Zhu, A. H. Trout, A. S. Ahmed, Y. K. Luo, C. H. Lee, M. R. Brenner, S. Rajan, J. A. Gupta, D. W. McComb *et al.*, *Nano Lett.* **18**, 3125 (2018).
- [56] R. Roldán, E. Cappelluti, and F. Guinea, *Phys. Rev. B* **88**, 054515 (2013).
- [57] N. F. Q. Yuan, K. F. Mak, and K. T. Law, *Phys. Rev. Lett.* **113**, 097001 (2014).
- [58] J. Yuan and C. Honerkamp, [arXiv:1504.04536](https://arxiv.org/abs/1504.04536).
- [59] Y.-T. Hsu, A. Vaezi, M. H. Fischer, and E.-A. Kim, *Nat. Commun.* **8**, 14985 (2017).
- [60] O. Zheliuk, J. Lu, Q. Chen, A. El Yumin, S. Golightly, and J. Ye, *Nat. Nanotechnol.* **14**, 1123 (2019).
- [61] Y. Saito, Y. Nakamura, M. S. Bahramy, Y. Kohama, J. Ye, Y. Kasahara, Y. Nakagawa, M. Onga, M. Tokunaga, T. Nojima *et al.*, *Nat. Phys.* **12**, 144 (2016).
- [62] R. Akashi, M. Ochi, S. Bordács, R. Suzuki, Y. Tokura, Y. Iwasa, and R. Arita, *Phys. Rev. Appl.* **4**, 014002 (2015).
- [63] R. Akashi, Y. Iida, K. Yamamoto, and K. Yoshizawa, *Phys. Rev. B* **95**, 245401 (2017).
- [64] S. Kanasugi and Y. Yanase, *Phys. Rev. B* **98**, 024521 (2018).
- [65] A. T. Rømer, T. A. Maier, A. Kreisel, I. Eremin, P. J. Hirschfeld, and B. M. Andersen, *Phys. Rev. Res.* **2**, 013108 (2020).
- [66] D. Costanzo, S. Jo, H. Berger, and A. F. Morpurgo, *Nat. Nanotechnol.* **11**, 339 (2016).
- [67] Y. Ge and A. Y. Liu, *Phys. Rev. B* **87**, 241408(R) (2013).
- [68] M. Rösner, S. Haas, and T. O. Wehling, *Phys. Rev. B* **90**, 245105 (2014).
- [69] T. Das and K. Dolui, *Phys. Rev. B* **91**, 094510 (2015).
- [70] D. Costanzo, H. Zhang, B. A. Reddy, H. Berger, and A. F. Morpurgo, *Nat. Nanotechnol.* **13**, 483 (2018).
- [71] K. S. Burch, D. Mandrus, and J.-G. Park, *Nature (London)* **563**, 47 (2018).
- [72] B. Huang, G. Clark, E. Navarro-Moratalla, D. R. Klein, R. Cheng, K. L. Seyler, D. Zhong, E. Schmidgall, M. A. McGuire, D. H. Cobden *et al.*, *Nature (London)* **546**, 270 (2017).
- [73] C. Gong, L. Li, Z. Li, H. Ji, A. Stern, Y. Xia, T. Cao, W. Bao, C. Wang, Y. Wang *et al.*, *Nature (London)* **546**, 265 (2017).
- [74] M. Nakano, Y. Wang, S. Yoshida, H. Matsuoka, Y. Majima, K. Ikeda, Y. Hirata, Y. Takeda, H. Wadati, Y. Kohama *et al.*, *Nano Lett.* **19**, 8806 (2019).